Mathematical model for laser ablation to generate nanoscale and submicrometer-size particles

A. Kar and J. Mazumder
Center for Laser-Aided Materials Processing, Mechanical and Industrial Engineering Department, University of Illinois at Urbana-Champaign, 1206 West Green Street, Urbana, Illinois 61801
(Received 13 October 1992)

Nanosize particles have several interesting features for synthesizing new materials with improved properties compared to the coarser-grained conventional materials, but the rate of production of such particles in various processes is usually very low. However, laser ablation is expected to give a higher yield. In this paper, a gas-dynamical model is developed for analyzing the plasma formation, and the velocity and particle-size distributions in the plasma during laser ablation. The melting and evaporation rates are determined by using the heat-conduction equation and the Stefan condition. To account for the discontinuity of various state variables across the Knudsen layer, jump conditions are used; the gas-dynamics equations are solved to study the convective flow of the metal particles in the region above the Knudsen layer. The plasma physics is used to model the formation of plasma and to compute the laser-beam attenuation coefficient and ion concentration in the plasma. The particle-size distribution in the plasma is determined by using a droplet-growth theory. Nanosize particles are found to exist near the vaporization front, and the particle size increases as one moves towards the plasma boundary. Similarly, the velocity of the particles is found to be higher at the plasma boundary than that inside the plasma.

PACS number(s): 81.35.+k, 47.40.−x, 44.25.+f, 44.30.+v

I. INTRODUCTION

The art of synthesizing new materials with improved properties lies in the ability to produce microstructures with atomic arrangements and/or chemical compositions that are different from those of conventional materials [1]. Rapid solidification techniques are usually used to produce novel metastable alloys with new chemical compositions. It should be noted that based on the atomic arrangements, the conventional materials can be classified as crystalline and amorphous which differ from each other in that the former has both short- and long-range orders, whereas the latter has only short-range and no long-range order. For this reason, nanocrystalline materials, which do not have any short- and long-range orders, are very important in the development of new materials. The atoms of a nanocrystal can be identified as "crystal atoms" and "boundary atoms" based on the nearest-neighbor configuration [1]. The "crystal atoms" have the nearest-neighbor configurations similar to the lattice configuration, whereas the nearest-neighbor configurations of the "boundary atoms" differ from the lattice configurations. More discussions on nanoscale materials can be found in Refs. [1–7].

The average grain size of nanocrystalline materials usually ranges from 5 to 25 nm, and a large fraction of the material is made up of grain boundaries containing most of the atoms. Due to the short-range disorder in the interfaces, which influences thermodynamic, magnetic, and electronic properties, and the small grain size, which affects sintering, plasticity, and diffusivity, the nanocrystalline materials have improved properties compared with the conventional coarser-grained materials. Studies on diffusion in nanocrystalline materials can be found in Refs. [8–11]. Horvath, Birringer, and Gleiter [8] measured the self-diffusivity of the radioisotope ^{67}Cu in nanocrystalline (8 nm) copper at 353 and 393 K, and found the respective diffusivity to be 2×10^{-18} and 1.7×10^{-17} m^2/s, which are, respectively, 16 and 14 orders of magnitude higher than the lattice self-diffusion coefficient, and about 2 and 3 orders of magnitude higher than the grain-boundary self-diffusivity. Enhanced solid solubility in nanocrystalline materials has been examined in Refs. [9,12]. Birringer *et al.* [9] showed that the solubility of Bi in nanocrystalline (8 nm) Cu is about 10^4 times the solubility of Bi in crystalline Cu. Rupp and Birringer [13] found that the specific heat of nanocrystalline (6 nm) palladium increases by about 29% and 53% compared with that of polycrystalline palladium at 150 and 300 K, respectively, and the increment is 9% at 150 K and 11% at 300 K for nanocrystalline (8 nm) copper. The thermal expansion coefficient of nanocrystalline (8 nm) copper has been found [1] to be twice the corresponding value of copper single crystals. Similarly, improved magnetic [2,7] and electrical [1] properties can be obtained by using nanoscale materials instead of the conventional coarser-grained materials. Mechanical properties, such as hardness, fracture stress, and low-temperature ductility, of nanocrystalline materials have been found [6,14–16] to improve relative to the conventional materials. Siegel *et al.* [17] showed that nanocrystalline (12 nm) TiO_2 (rutile) can be sintered without using any compacting or sintering agent, such as polyvinyl alcohol which is usually required, at atmospheric pressure and 400 °C lower temperatures than coarse-grained TiO_2. Karch, Birringer, and Gleiter [14] used nanoscale ceramic particles to produce ductile ceramics that can undergo large plastic deformations at room temperature due to the diffusional flow of atoms along the intercrystalline interfaces. Such creep enhancement may be explained by

using Coble's [18] creep model, according to which the deformation rate $\dot{\epsilon}$ of diffusional creep by interfacial diffusion is proportional to D_b/d^3, where D_b is the grain-boundary diffusivity and d is the average grain size, and, therefore, $\dot{\epsilon}$ is expected to increase because D_b and d are very large and small, respectively, for nanocrystalline materials. However, Nieman, Weertman, and Siegel [19,20] showed that the creep rates are at least three orders of magnitude smaller than Coble's model predictions for nanoscale Pd and Cu at room temperature.

The improved properties of nanocrystals have drawn considerable interest in developing methods for producing these materials in large quantities, because the yields of various techniques have been found to be very low. Birringer *et al.* [21] devised a gas condensation technique in which particles are produced by vaporizing the metal inside a vacuum chamber, and then collected at the surface of a liquid-nitrogen-cooled cold finger. Siegel *et al.* [17] used the gas condensation technique [21] to produce nanoparticles of TiO_2. Chow *et al.* [22] synthesized nanocomposites (3–12-nm average particle size) at high pressure (0.1–5 Torr) by maintaining a temperature gradient between a cold substrate and a hot source to cause sputtering of the source. By magnetron sputtering, Hahn and Averback [23] produced nanocrystalline particles of pure metals, binary alloys, intermetallics, and ceramics with average grain size ranging from 7 to 50 nm. Jervis and Zocco [24] used the photolytic laser chemical-vapor-deposition technique to generate nanoscale Fe_3C particles with average size 5.7 nm. Matsui *et al.* [25] fabricated a tungsten rod of 15 nm diameter on a silicon substrate by using electron-beam-induced surface reaction. Baba *et al.* [26] produced ultrafine AlN powder by rf plasma method. Andres *et al.* [27] gave an excellent report on various methods for producing nanocrystalline materials. Besides these techniques, laser ablation can also be used to produce nanophase materials. In fact, laser ablation, sputtering, electron beam, or rf plasma methods can provide better control of the evaporation process, do not require any high melting point container and, therefore, can be used to produce nanoscale particles of refractory or reactive elements, and are suitable for generating nanocrystalline multicomponent or composite materials.

It can be seen from the literature that laser ablation studies are mainly concerned with the deposition of thin films of various materials, diagnostics of the plasma formed during ablation, and mathematical modeling of the ablation process. Zweig [28] presented a thermomechanical model for laser ablation to explain the experimental drilling-depth and recoil data. Kelly and Braren [29] used the gas-dynamics approach to model the laser-induced sputtering of polymers. Various gas-dynamics processes, which occur during the laser heating of a substance, were investigated in Refs. [30,31]. Also, the nonequilibrium phenomena in a laser-induced plasma near a solid surface were studied by Kozlov *et al.* [32]. Batanov *et al.* [33] examined the mechanisms of vapor formation from solid targets during laser irradiation and pointed out that the evaporation is from the liquid metal, that is, a liquid film exists during irradiation. Gai and Voth [34] presented a computer simulation technique for laser ablation of polymers. Kools *et al.* [35] studied the gas flow dynamics to model the laser ablation deposition of thin films. Dahmani [36] used experimental data to correlate the ablated mass flux and ablation pressure with the absorbed laser intensity, laser wavelength, and target atomic number. Singh and Narayan [37] presented a model to study the pulsed-laser evaporation technique for thin-film deposition.

The physics of laser ablation involves many phenomena—such as the target-laser interactions, vaporization process, plasma formation and its interaction with the laser beam, and nucleation for the formation of particles of different sizes—which have to be modeled properly in order to understand the effects of various laser parameters on the formation of nanocrystalline particles. The purpose of this paper is to develop a mathematical model for determining the particle-size distribution in the plasma formed during laser ablation. To achieve this objective, the heat conduction equation, Stefan condition, vaporization physics, gas dynamics equations, plasma physics, and droplet-growth theory are used in this paper.

II. MATHEMATICAL MODEL

A. Process physics

Although laser ablation is mostly used for the deposition of thin films, it can be used to produce nanoscale particles. In this technique, a target, which is made up of the material whose nanocrystalline particles are of interest, and a cold substrate, which is usually cooled with liquid nitrogen, are placed in a vacuum chamber, and the target is irradiated with a high-intensity laser beam. When the laser beam interacts with the target, a part of the beam is reflected, and the rest is absorbed by the atoms of the target material giving rise to thermal energy to cause heating, melting, and vaporization of the target. The vapor also absorbs a portion of the laser beam, which raises its temperature and eventually leads to the formation of plasma. A schematic representation of various phenomena that occur during laser ablation is given in Fig. 1. The particles produced due to the irradiation of the target interact among one another in the vapor and plasma phases to produce the clusters of different sizes, which are collected at the surface of the cold substrate.

B. Mathematical formulations

The process of nanoscale particle formation during laser ablation is modeled as follows by using the axisymmetric coordinate system shown in Fig. 1.

1. Heat transfer in the solid target

The thermal energy generated due to the laser-target interactions is considered to propagate through the solid region of the target by axial conduction only, because the radial heat conduction is usually very small [32] within a wide range of the laser-beam diameters and pulse durations. Therefore, the governing equation can be written as

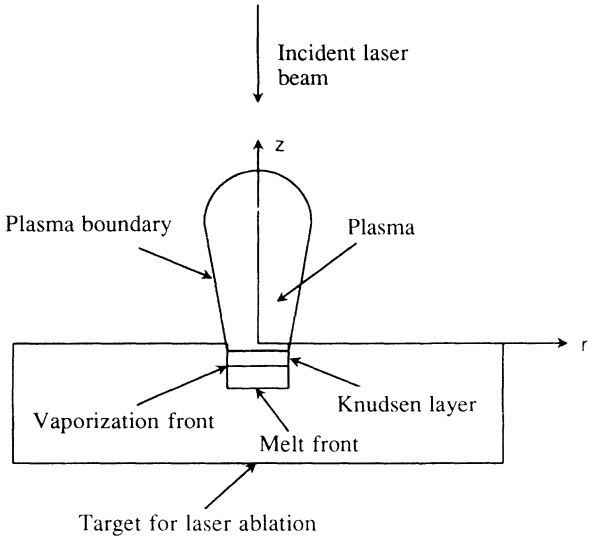

FIG. 1. A schematic representation of the process physics during laser ablation.

$$\frac{\partial T_s}{\partial t}=\alpha_s\frac{\partial^2 T_s}{\partial z^2} \quad \text{for } -\infty \le z \le s_2(t) \text{ and } t>0 \ . \tag{1}$$

Here, T_s and α_s are, respectively, the temperature and thermal diffusivity of the solid target, t is the time variable, and $s_2(t)$ represents the location of the melt front, that is, the solid-liquid interface such that $s_2(t)\le 0$.

Equation (1) has to be solved subject to the following initial and boundary conditions:

$$T_s(z,0)=T_0 \ , \tag{2a}$$

$$T_s(-\infty,t)=T_0 \ , \tag{2b}$$

and

$$T_s[s_2(t),t]=T_m \ , \tag{2c}$$

where T_0 and T_m are, respectively, the initial and melting temperature of the target. The melt-front location $s_2(t)$ can be determined by using the following Stefan condition:

$$k_l\frac{\partial T_l}{\partial z}-k_s\frac{\partial T_s}{\partial z}=-\rho_s L_m\frac{ds_2}{dt} \quad \text{at } z=s_2(t) \ , \tag{2d}$$

which is subject to the condition

$$s_2(0)=0 \ . \tag{2e}$$

Here, k_l and k_s are the thermal conductivities of the liquid and solid phases of the target material, respectively; T_l is the temperature in the liquid region of the target; ρ_s is the density of the solid target; and L_m is the latent heat of melting of the target material.

2. Heat transfer in the liquid region

The liquid film formed during laser ablation is very thin [33] within which the temperature can be considered to vary linearly such that

$$T_l(z,t)=T_L+\frac{z-s_1(t)}{s_2(t)-s_1(t)}(T_m-T_L) \ . \tag{3}$$

Here, $T_l(z,t)$ is the temperature distribution in the liquid region of the target, and T_L is the saturation temperature at the vaporization front, that is, at the liquid-vapor interface whose location is represented by $s_1(t)$, where $s_1(t)\le 0$. The vaporization front location, $s_1(t)$ can be determined by using the following Stefan condition:

$$I-k_l\frac{\partial T_l}{\partial z}=-\rho_{Li}\left[L_v+T_g\frac{5R_g}{2M_g}-T_L C_{pL}+\tfrac{1}{2}v_g^2\right]\frac{ds_1}{dt} \tag{4a}$$

at $z=s_1(t)$, which is subject to the condition

$$s_1(0)=0 \ . \tag{4b}$$

Here, I is the intensity of the incident laser beam (see Fig. 1), ρ_{Li} is the density of the material in the liquid layer at the vaporization front, L_v is the latent heat of vaporization of the target material, T_g is the temperature of the gas at the top plane of the Knudsen layer, R_g is the universal gas constant, M_g is the molecular weight of the target material, C_{pL} is the specific heat of the vapor in the Knudsen layer at the vaporization front at constant pressure, and v_g is the speed of the gas at the top plane of the Knusden layer. It should be noted that the Stefan condition (4a) is written by assuming that the vaporization rate is very much higher than the condensation rate at the liquid-vapor interface.

3. Jump conditions

The state variables, that is, temperature, pressure, density, and velocity, are discontinuous across the Knudsen layer. To account for such discontinuity, the following jump conditions [32] are used in this study, which are valid in the range $0\le v_g\le c_g$, where c_g is the speed of sound in the region above the Knudsen layer:

$$\frac{\rho_g}{\rho_L}=\frac{0.397m^3-0.6015m^2+0.191m+1}{1.183m^3-0.154m^2+2.284m+1} \ , \tag{5a}$$

$$\frac{T_g}{T_L}=\frac{2.643m^3-6.939m^2+2.706m+1}{-0.3636m^3-4.4595m^2+2.7058m+1} \ , \tag{5b}$$

where ρ_g is the density of the gas at the top plane of the Knudsen layer, ρ_L is the density of the vapor in the Knudsen layer at the vaporization front, and $m=v_g/(2R_gT_L/M_g)^{1/2}$ in which v_g can be expressed in terms of other variables by using the following mass-conservation equation:

$$\rho_{Li}|ds_1/dt|=\rho_g v_g \ . \tag{5c}$$

4. Gas-dynamics equations

The flow of metal particles in the region above the Knudsen layer is modeled by using the following unsteady two-dimensional axisymmetric gas-dynamics equations [32]:

$$\frac{\partial}{\partial t}\bar{U}+\frac{\partial}{\partial r}\bar{F}+\frac{\partial}{\partial z}\bar{G}=\bar{S}\ , \tag{6}$$

where

$$\bar{U}=\begin{bmatrix} r\rho \\ r\rho u \\ r\rho v \\ r\rho E \end{bmatrix},$$

$$\bar{F}=\begin{bmatrix} r\rho u \\ -(\gamma-3)r\rho u^2/2+(\gamma-1)r\rho(E-v^2/2) \\ r\rho uv \\ \gamma r\rho uE-(\gamma-1)r\rho u(u^2+v^2)/2 \end{bmatrix},$$

$$\bar{G}=\begin{bmatrix} r\rho v \\ r\rho uv \\ -(\gamma-3)r\rho v^2/2+(\gamma-1)r\rho(E-u^2/2) \\ \gamma r\rho uvE-(\gamma-1)r\rho v(u^2+v^2)/2 \end{bmatrix},$$

and

$$\bar{S}=\begin{bmatrix} 0 \\ (\gamma-1)\rho\{E-(u^2+v^2)/2\} \\ 0 \\ -r(\nabla\cdot\bar{S}_1+\partial I/\partial z) \end{bmatrix}.$$

Here, ρ, u, v, and E represent, respectively, the density, velocity in the r direction, velocity in the z direction, and total energy per unit mass of a particle at any time t and location (r,z) in the region above the Knudsen layer. γ is the specific-heat ratio, $\nabla\cdot\bar{S}_1$ represents the loss of energy from unit volume in unit time due to radiation, and $\partial I/\partial z$ accounts for the absorption of laser energy in unit volume in unit time due to the attenuation of the laser beam as it passes through the plasma and gas-vapor phases.

In order to determine $\nabla\cdot\bar{S}_1$, the plasma is considered to be optically thin in this study, which is a good approximation when the volume of the plasma is very small and leads to the following expression [38] for $\nabla\cdot\bar{S}_1$:

$$\nabla\cdot\bar{S}_1=4k\sigma T^4\ , \tag{7a}$$

where k is the absorption coefficient, σ is the Stefan-Boltzmann constant, and T is the temperature in degrees Kelvin.

By noting that the spectral absorption coefficient $K_\nu=N_n\sigma_{\nu n}+N_i\sigma_{\nu i}$, where N_n and N_i are, respectively, the number densities of the neutrals and ions, and $\sigma_{\nu n}$ and $\sigma_{\nu i}$ are, respectively, the spectral absorption cross sections of the neutrals and ions, and by using Kramers' formula [38], k can be written as

$$k=\frac{15}{\pi^4}\frac{7.9\times10^{-18}}{(k_BT)^3}\left[\frac{I_1^3N_n}{Z^2}+\frac{I_2^3N_i}{(Z-1)^2}\right]\ \text{cm}^{-1} \tag{7b}$$

for the first quantum state of the material. Here k_B is the Boltzmann constant, Z is the atomic number, and I_1 and I_2 are, respectively, the first and second ionization potentials of the material in eV. The amount of laser energy absorbed in unit volume of the plasma in unit time is given by

$$\frac{\partial I}{\partial z}=-I^*(r,t)ke^{-kz}\ , \tag{7c}$$

where $I^*(r,t)$ represents the radial and temporal distribution of the laser intensity. Equation (6) has to be solved subject to the initial and boundary conditions. At $t=0$, the variables ρ, u, v, and E are taken to be zero. At $r=0$, the symmetric condition is applied, that is, $\partial\rho/\partial r$, $\partial u/\partial r$, $\partial v/\partial r$, and $\partial E/\partial r$ are equal to zero. At $z=0$, ρ, u, v, and E are, respectively, ρ_g, 0, v_g, and E_g, where

$$E_g=R_gT_g/[(\gamma-1)M_g]+v_g^2/2\ .$$

5. *Ion concentration in the plasma*

Although the unsteady gas-dynamics equations are used to study the velocity, temperature, and density distributions in the plasma, the plasma is considered to be in local thermodynamic equilibrium so that the Saha equation [38] can be applied to determine the ion concentration. It should be noted [38] that the gas is usually singly ionized in the temperature range 8000–30 000 K and that the second ionization does not occur in this temperature range because the second ionization potential is approximately twice the value of the first ionization potential. By considering that the ionized particles are in the singly ionized state and by taking the statistical weights to be unity in the Saha equation, the ion mass fraction m_i can be shown to be

$$m_i=[(A^2+4\rho A)^{1/2}-A]/(2\rho)\ , \tag{8}$$

where

$$A=8\times10^{-9}M_gT^{3/2}\exp[-I_1/(k_BT)]\ .$$

6. *Particle-size distribution*

In order to understand the effects of various laser parameters on the diameters of the particles formed during laser ablation, the droplet-growth theory of Lifshitz and Slyozov [39] is used to determine the particle-size distribution in the plasma. According to this theory, the mean diameter of a cluster, $D_c(t)$, is given by

$$D_c(t)=(32\alpha Dt/9)^{1/3}\ . \tag{9}$$

Here, D is the mass diffusion coefficient and $\alpha=2\sigma_t v'C_{0\infty}/(k_BT)$, where σ_t is the surface tension, v' is the molecular volume of the droplet material, and $C_{0\infty}$ is the concentration of the saturated solution which is defined in terms of the volume of the material dissolved in unit volume of the solution. Although Eq. (9) is used in this study, it should be noted that the detailed condensation processes and the arrangement of chemical bonds are very important in the formation of the clusters.

C. Method of solution

1. Determination of s_1, s_2, and δ

Equation (1) is solved by using the integral method to obtain the following temperature distribution:

$$\frac{T_s(z,t)-T_0}{T_m-T_0}=1-\frac{3}{2}\frac{z-s_2}{\delta-s_2}+\frac{1}{2}\left[\frac{z-s_2}{\delta-s_2}\right]^3 , \tag{10}$$

where the location of the thermal boundary layer $\delta(t)$ is given by

$$\frac{d\delta}{dt}=\frac{4\alpha_s}{\delta-s_2}-\frac{5}{3}\frac{ds_2}{dt} , \tag{11}$$

which is subject to the condition $\delta(0)=0$.

To determine s_1, s_2, and δ, Eqs. (2d), (4a), and (11) are discretized over a time step Δt by using the finite difference approximation to obtain the following equations:

$$\delta=s_2-\frac{8}{3}\left[(s_2-s_2')+\left\{(s_2-s_2')^2-\frac{9\bar{C}}{64}\right\}^{1/2}\right] , \tag{12a}$$

$$s_2=\frac{A_c s_1+A_b\delta+(s_2-s_2')(s_2-s_1)(\delta-s_2)}{A_c+A_b} , \tag{12b}$$

$$s_1=\frac{-k_l(T_m-T_L)\Delta t+Is_2\Delta t+(s_2s_1'+s_1^2)K_2^*}{I\Delta t+(s_2+s_1')K_2^*} . \tag{12c}$$

Here,

$$\bar{C}=-8\alpha_s\Delta t-(\delta'-s_2')^2 ,$$

$$A_c=\tfrac{3}{2}k_s(T_0-T_m)\frac{\Delta t}{\rho L_m} ,$$

$$A_b=k_l(T_m-T_L)\frac{\Delta t}{\rho L_m} ,$$

$$K_2^*=-\rho_{Li}\left[L_v+\frac{5}{2}\frac{R_gT_g}{M_g}-T_LC_{pL}+\tfrac{1}{2}v_g^2\right] ,$$

and δ', s_1', and s_2' represent the functions $\delta(t-\Delta t)$, $s_1(t-\Delta t)$, and $s_2(t-\Delta t)$, respectively. At any time t, the variables δ, s_1, and s_2 are determined from Eqs. (12a), (12b), and (12c) by using the method of successive iteration.

2. Determination of ρ_g, v_g, and E_g

The jump conditions (5a) and (5b) have to be used in order to determine the boundary conditions, that is, the values of ρ_g, v_g, and E_g for the gas dynamics (6). But these jump conditions have two unknowns ρ_L and T_L, which are determined by using the kinetic theory of vaporization, the Clausius-Clapeyron equation, and the ideal-gas law. The expression for T_L is found to be

$$\rho_{Li}\left|\frac{ds_1}{dt}\right|=\left[\frac{M_g}{2\pi R_gT_L}\right]^{1/2}P_0\exp\left\{\frac{L_v}{R_g}\left[\frac{1}{T_0}-\frac{1}{T_L}\right]\right\} , \tag{13}$$

where P_0 is the vapor pressure at any saturation temperature T_0. T_L is obtained from expression (13) by using the method of bisection. After determining T_L, the vapor pressure in the Knudsen layer at the vaporization front, P_L, is obtained by using the Clausius-Clapeyron equation, and then ρ_L is determined from the ideal-gas law. Now ρ_g, T_g, and v_g can be obtained from the conditions (5a), (5b), and (5c), and then E_g is determined by using the relation

$$E_g=R_gT_g/[(\gamma-1)M_g]+v_g^2/2$$

in order to solve Eq. (6).

3. Determination of ρ, u, v, T, m_i, and $D_c(t)$

The gas dynamics (6) is solved by using Lax's explicit method [40], which leads to the following discretization of Eq. (6):

$$\begin{aligned}\bar{U}_{i,j}^{n+1}=&\tfrac{1}{4}(\bar{U}_{i+1,j}^n+\bar{U}_{i-1,j}^n+\bar{U}_{i,j+1}^n+\bar{U}_{i,j-1}^n)\\&-\frac{\Delta t}{2\Delta r}(\bar{F}_{i+1,j}^n-\bar{F}_{i-1,j}^n+\bar{G}_{i,j+1}^n-\bar{G}_{i,j-1}^n)\\&+\frac{\Delta t}{4}(\bar{S}_{i+1,j}^n+\bar{S}_{i-1,j}^n+\bar{S}_{i,j+1}^n+\bar{S}_{i,j-1}^n)\end{aligned} \tag{14}$$

for $n=0,1,2,\ldots$, $i=1,2,3,\ldots$, and $j=1,2,3,\ldots$. In Eq. (14), the radial mesh size Δr is taken equal to the axial mesh size Δz and the indices i, j, and n are used to represent the discretized values of r, z, and t, respectively, such that

$$X_{\eta,\xi}^{\tau}=X(\eta\Delta r,\xi\Delta z,\tau\Delta r) ,$$

where $X=\bar{U}$, $\bar{F}$, $\bar{G}$, and $\bar{S}$; $\tau=0,1,2,\ldots$; $\eta=0,1,2,\ldots$, and $\xi=0,1,2,\ldots$.

Expressions (7a), (7b), and (7c) are used in Eq. (14) in order to determine the distributions of density ρ, radial velocity u, axial velocity v, and temperature T in the plasma. After this, the ion mass fraction m_i and the particle-size distribution $D_c(t)$ are calculated by using Eqs. (8) and (9), respectively.

III. RESULTS AND DISCUSSION

The above-mentioned mathematical model is used to investigate the effects of various laser parameters on the production of nanocrystalline particles of niobium during laser ablation. A KrF excimer laser of wavelength 0.248 μm is used in this study to ablate a niobium target in a vacuum chamber of pressure 10^{-7} Torr. The laser-beam radius is taken to be 0.798 mm, and the laser intensity is considered to be radially uniform but varies with time with a repetition rate of 50 Hz and a pulse-on time of 30 ns. With these parameters, results are obtained for the laser energies 300, 400, and 500 mJ/pulse which corresponds to the intensities 499.8, 666.4, and 833.1 MW/cm^2, respectively. Also, due to the unavailability of the absorptivity data, the absorptivity is taken to be 60% in all of the calculations unless stated otherwise.

Figures 2 and 3 represent the locations of the solid-liquid and liquid-vapor interfaces, respectively, during

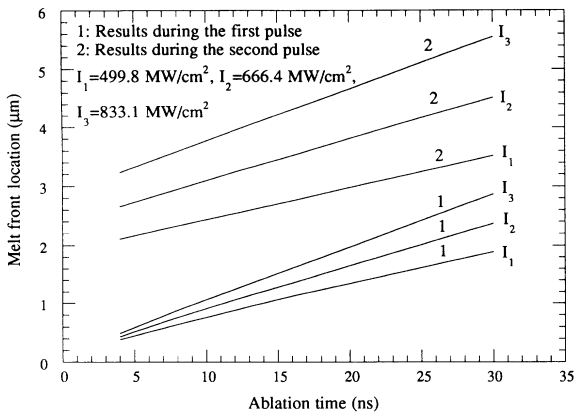

FIG. 2. Variation of the solid-liquid interface depth with ablation time.

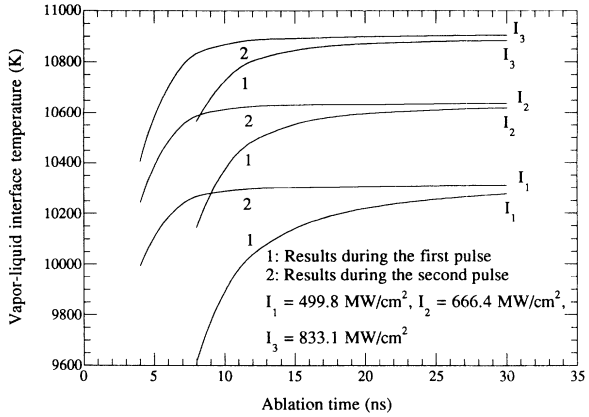

FIG. 4. Variation of the vapor-liquid interface temperature with ablation time.

laser ablation for three different intensities. It should be noted that these two figures look almost identical, that is, the location of the melt front is very close to that of the vaporization front, which implies that the liquid film is very thin. In these figures as well as in Figs. 4 and 5, the lines 1 and 2 are the results for the first and second pulses, respectively, and the ablation time is measured by taking the time to be zero at the beginning of each pulse, such that the actual time, $t_{\text{act}}=(n-1)\tau+t_f$, where n is the number of pulses, τ is the period of the pulses, and t_f is the ablation time reported in the figures. It can be seen from Figs. 2 and 3 that more material melts and vaporizes as the laser intensity increases, or as the ablation time increases for a given intensity. It should be noted that the amount of vapor produced during vaporization is directly proportional to the depth of the vaporization front and, therefore, Fig. 3 indicates that a very small amount of material vaporizes during one laser pulse.

Figure 4 shows the temperature at the vaporization front during the first and second pulses for various laser intensities. The temperature at the vapor-liquid interface increases as the laser intensity increases. With respect to the ablation time, the vaporization-front temperature increases rapidly during the initial stage of the pulse, and then becomes constant near the end of the pulse. The amount of vapor produced at the vaporization front in unit area per unit time is reported in Fig. 5 which shows that the vapor flux is rather large. Although the depth of the vaporization front created during one laser pulse is very small (see Fig. 3), a large vapor flux is expected, because the vaporization occurs during a few nanoseconds. Figure 5 shows that the vapor flux increases as the laser intensity increases, and it increases rapidly during the first several nanoseconds of the ablation period to eventually reach a constant value.

Figures 6 and 7 show the variations of radial and axial velocities with radius at various heights in the plasma at the end of the first pulse, that is, at the ablation time $t=30$ ns. Both figures show that the velocity increases as height z increases. However, the radial velocity u increases slowly with z compared with the axial velocity v. On the other hand, u increases more rapidly with r than v. It should be noted that the values of u and v vary from a few to several hundred meters per second, which may seem to be too high. But such high velocities are not unrealistic because the particles have been experimentally found to move in the plasma with such high [41,42] and, in many cases, even higher [43,44] velocities during laser

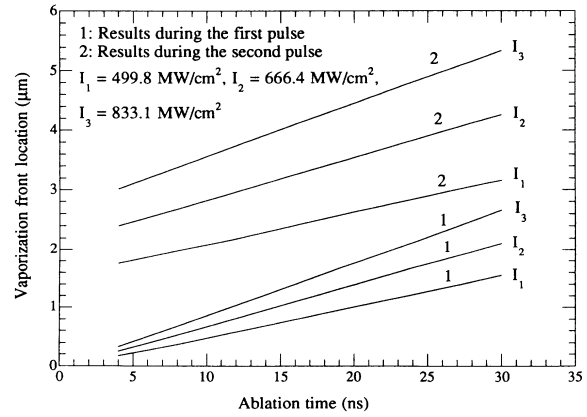

FIG. 3. Variation of the vapor-liquid interface depth with ablation time.

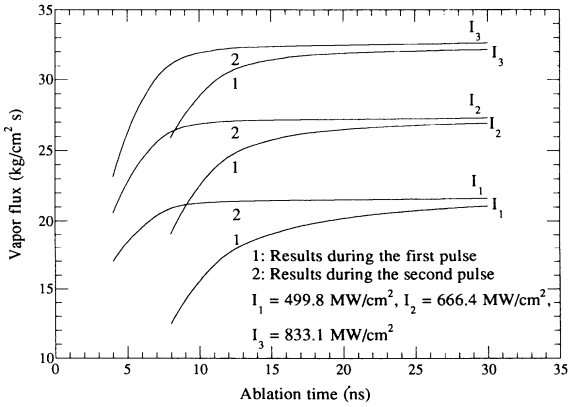

FIG. 5. Variation of the flux of vapor at the surface of the liquid with ablation time.

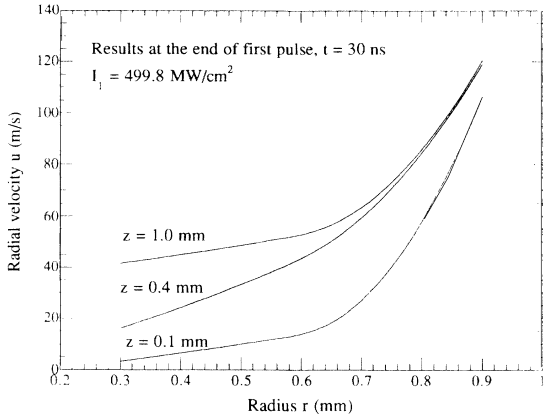

FIG. 6. Radial velocity distribution of particles in the plasma.

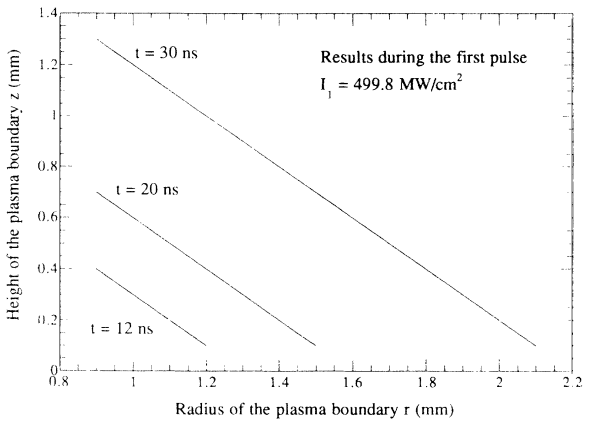

FIG. 8. Propagation of the plasma boundary during laser ablation.

ablation. The values of v oscillate near the end of each curve in Fig. 7, because the variables ρ, u, v, and T are discontinuous at the plasma boundary and the numerical scheme used in this study cannot resolve this discontinuity. For this reason, each of the three curves of Fig. 7 has the same V-shaped structure at the end.

Figure 8 shows the coordinates, that is, the values of r and z, of the plasma boundary for the ablation times $t=12$, 20, and 30 ns during the first laser pulse. The lines in the figure represent a portion of the plasma boundary and demonstrate the evolution of the plasma volume as the ablation time increases. Thus the present model can be used to study the growth of the plasma during laser ablation. Figure 9 shows the variation of temperature with radius at various heights in the plasma at the end of the first pulse, which is also strongly affected by the discontinuity at the plasma boundary as in the case for Fig. 7. For this reason, the rightmost portions of the curves in Figs. 7 and 9 show the effect of this discontinuity rather than any physically realistic values for the velocity and temperature, respectively. Figure 10 presents the radial variation of the ion mass fraction at various heights in the plasma. The ion mass fraction increases as r or z increases, that is, as one moves towards the plasma boundary. This is because the density of the plasma is less at the plasma boundary than that at the plasma base near the target surface. It can be seen from Fig. 10 that the ion mass fraction is very low in the plasma, which means that the plasma contains mainly neutrals, that is, a weakly ionized plasma is formed.

Figures 11, 12, and 13 show the distributions of the particle diameter in the plasma. Tadashi *et al.* [45] have observed 20 nm particles during Q-switched Nd: YAG (neodymium-doped yttrium aluminum garnet) laser ablation. In Fig. 11, the variation of the particle size with the radius is shown for different ablation times $t=12$, 20, and 28 ns at the height $z=0.1$ mm, whereas Fig. 12 shows the variation of the particle size with r at various heights in the plasma at the end of the first pulse, that is, at the ablation time $t=30$ ns. Both Figs. 11 and 12 indicate that the particle size increases as r increases. Also, it can be observed from Figs. 11 and 12 that the particle size increases as the ablation time t or the height z increases. This can be understood by noting that the tiny vapor clusters, which originate at the vaporization front, undergo a lot of collisions as they flow towards the plasma boundary and as the ablation time, that is, the residence

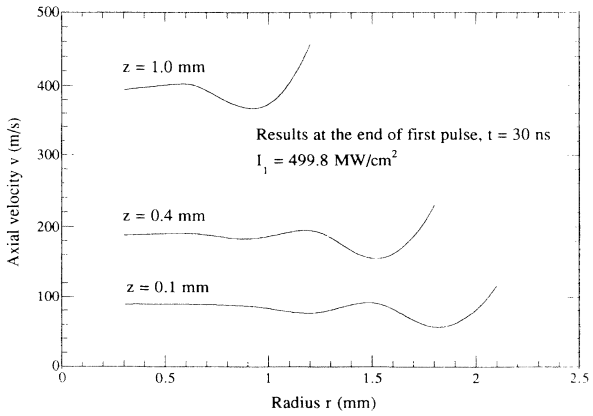

FIG. 7. Axial velocity distribution of particles in the plasma.

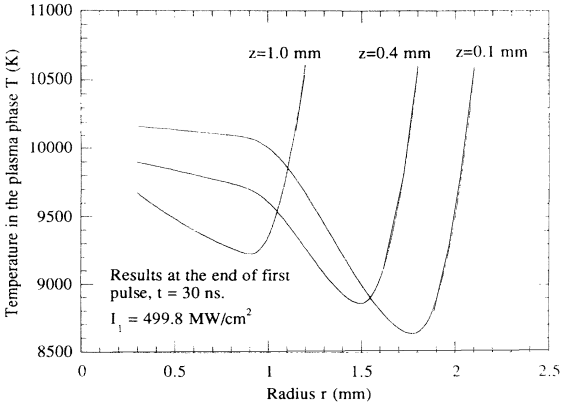

FIG. 9. Temperature distribution in the plasma phase during laser ablation.

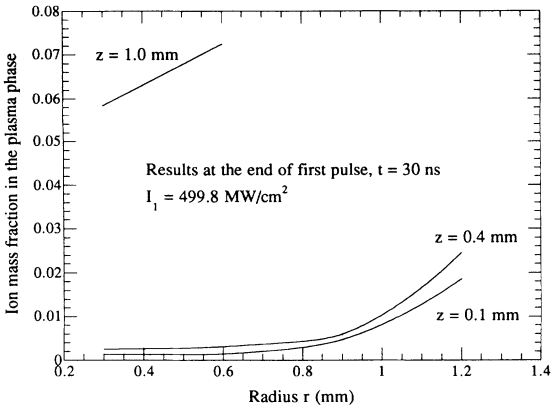

FIG. 10. Distribution of ion mass fraction in the plasma phase.

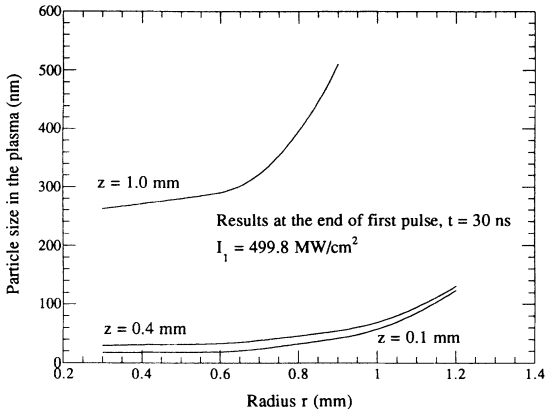

FIG. 12. Distribution of particle size at various heights in the plasma phase.

time of the particles in the plasma, increases. As a consequence of such collisions, the vapor clusters agglomerate to form larger particles.

It should be noted that the results of Figs. 2–12 are calculated by considering the absorptivity to be 60%. In order to examine the effects of absorptivity, the particle size distributions are obtained for three different values of the absorptivity as shown in Fig. 13, which indicates that the particle size is practically unaffected by the chosen values of the absorptivity.

Experimental verification

Besides obtaining the above-mentioned results for Nb, the model of this paper is used to study the ablation rates, that is, the evaporation rates, of Cr, Ni, and Pb for various laser energy densities, and the results are compared with experimental data of Ref. [46] as shown in Fig. 14. It can be seen from this figure that the theoretical predictions are higher than the experimental data. To understand this discrepancy, the maximum ablation rates for Cr, Ni, and Pb are calculated by using the following simple energy balance:

$$N^* = \frac{A_v A_t E_p}{\pi M_g r_0^2 [C_{ps}(T_m - T_0) + L_m + C_{pl}(T_v - T_m) + L_v]} , \tag{15}$$

where N^* represents the maximum ablation rate in terms of the number of atoms per unit pulse per unit area, A_v is Avogadro's number, A_t is the absorptivity of the target for the incident laser beam, E_p is the energy per pulse of the laser beam, r_0 is the laser-beam radius at the target surface, and C_{ps} and C_{pl} are the specific heats of the target in solid and liquid phases, respectively. Equation (15) is written by considering that the incident laser energy is utilized only to raise the temperature of the mass of ablated material from room temperature to its boiling temperature and supply the necessary latent heats of melting and boiling. Also, N^* represents the maximum ablation rate, because the energy losses due to conduction in the target, absorption and scattering in the plasma and vapor phases, conversion of thermal energy into the kinetic energy of the ablated particles, and the conduction, convec-

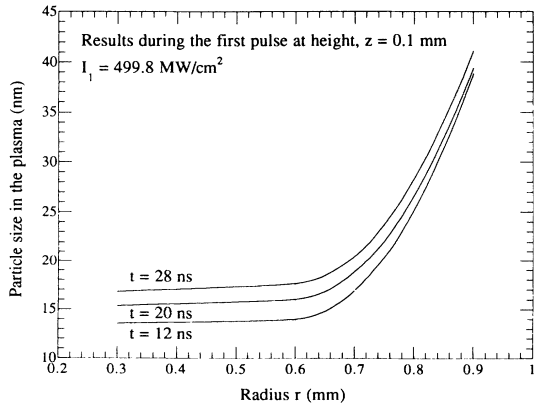

FIG. 11. Distribution of particle size in the plasma phase during laser ablation.

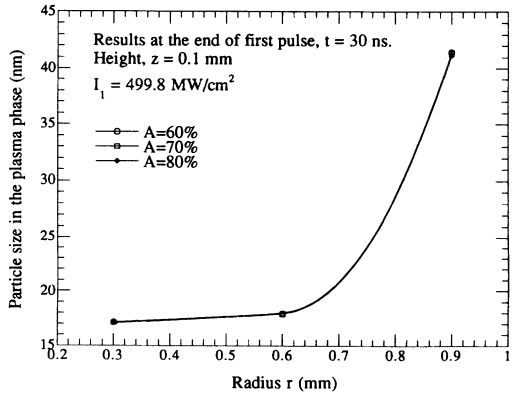

FIG. 13. The effects of absorptivity on the particle-size distribution in the plasma phase.

tion, and radiation losses from the target surface are not taken into account in Eq. (15).

The results obtained from Eq. (15) are plotted in Fig. 14 to show that the predictions of this model are lower and closer to the experimental data than the maximum values of the ablation rates, which means that the energy-loss terms are very important in the accurate determination of the ablation rates. Since the present model is based on one-dimensional heat conduction in the target and no conduction, convection, and radiation losses from the target surface, the results of this model are expected to be higher than the experimental data. Also, the lack of data, such as the values for thermophysical and optical properties at high temperatures, could be another reason for the discrepancy between the theoretical and experimental results. However, Fig. 14 shows that the maximum ablation rates, and the theoretical and experimental results, are qualitatively in good agreement because they vary in the same way as the laser energy density increases. For a given laser energy density, the trend that the ablation rate increases progressively for Cr, Ni, and Pb targets, respectively, which is predicted by the experimental data, is also predicted by this model. But the results obtained from Eq. (15) show that the maximum ablation rate is higher for Cr than that for Ni, which implies that the energy losses are higher for Cr than that for Ni during the ablation, since Cr ablates slower than Ni when the energy losses are taken into account.

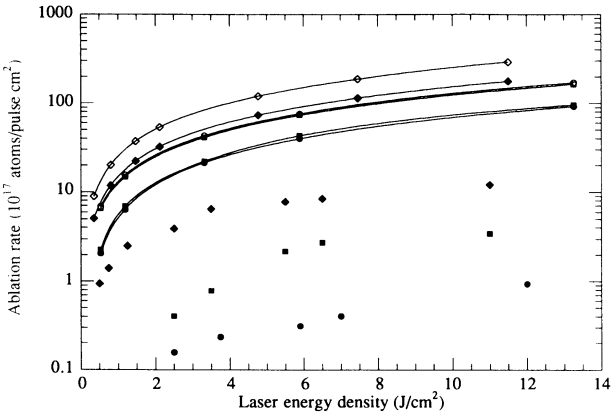

FIG. 14. Comparison between calculated ablation rates and experimental data: ● : Cr, experimental data; -●-: Cr, this model; -⊖-: Cr, maximum value; ■ : Ni, experimental data: -■-: Ni, this model; -⊟-: Ni, maximum value; ♦ : Pb, experimental data; -◆-: Pb, this model; -◇-: Pb, maximum value.

IV. CONCLUSION

A mathematical model is presented and applied to study the production of nanoscale niobium particles during laser ablation. The model is developed by considering heat conduction, the Stefan condition, vaporization physics, gas dynamics, plasma physics, and droplet-growth theory, and the results can be summarized as follows.

(1) More material melts and vaporizes as the laser intensity or the ablation time increases. Only a very small amount of material vaporizes during one laser pulse, but an extremely large vapor flux is generated.

(2) The temperature and vapor flux at the vaporization front increase rapidly during the first several nanoseconds of the pulse and then become constant near the end of the pulse.

(3) The radial and axial velocities vary from a few to several hundred meters per second.

(4) A weakly ionized plasma is formed, and the ion mass fraction increases as one moves towards the plasma boundary.

(5) Nanoscale particles exist near the vaporization front. The particle size increases as one moves towards the plasma boundary, or as the residence time of the particles in the plasma increases.

(6) The energy losses due to conduction in the target, absorption and scattering in the plasma and vapor phases, conversion of thermal energy into the kinetic energies of the ablated particles, and the conduction, convection, and radiation losses from the target surface are very important in the accurate determination of the ablation rates.

(7) The trend between the theoretical and experimental results is similar, but the theoretical predictions are higher than the experimental data, which could be due to the multidimensional energy losses and the lack of high-temperature data.

ACKNOWLEDGMENT

This work was made possible by a grant from the Air Force Office of Scientific Research (Grant No. F49620-92-J-0142).

[1] R. Birringer and H. Gleiter, *Encyclopedia of Materials Science and Engineering,* edited by R. W. Cahn (Pergamon, Oxford, 1988), Suppl. Vol. 1, p. 339.

[2] R. Birringer, U. Herr, and H. Gleiter, Trans. Jpn. Inst. Met. **27** (Suppl.), 43 (1986).

[3] H. Gleiter, in *Deformation of Polycrystals: Mechanisms and Microstructures,* edited by N. Hansen, A. Horsewell, T. Leffers, and H. Lilholt (Riso National Laboratory, Roskilde, Denmark, 1981), p. 15.

[4] C. G. Granquist and R. A. Buhrman, J. Appl. Phys. **47**, 2200 (1976).

[5] C. Hayashi, Phys. Today **40** (12), 44 (1987).

[6] R. W. Siegel and H. Hahn, in *Current Trends in the Physics of Materials,* edited by M. Yussouff (World Scientific, Singapore, 1987), p. 403.

[7] J. A. Cowan, B. Stolzmann, R. A. Averback, and H. Hahn, J. Appl. Phys. **61**, 3317 (1987).

[8] J. Horvath, R. Birringer, and H. Gleiter, Solid State Com-

mun. **62**, 319 (1987).
[9] R. Birringer, H. Hahn, H. Höfler, J. Karch, and H. Gleiter, Defect and Diffusion Forum **59**, 17 (1988).
[10] H. Hahn, J. H. Höfler, and R. S. Averback, Defect and Diffusion Forum **66-69**, 549 (1989).
[11] J. Horvath, Defect and Diffusion Forum **66-69**, 207 (1989).
[12] T. Mütschele and R. Kirchheim, Scr. Metall. **21**, 135 (1987).
[13] J. Rupp and R. Birringer, Phys. Rev. B **36**, 7888 (1987).
[14] J. Karch, R. Birringer, and H. Gleiter, Nature (London) **330**, 556 (1987).
[15] H. G. F. Wilsdorf. O. T. Inal, and L. E. Murr, Z. Metall. **69**, 701 (1978).
[16] M. J. Mayo, R. W. Siegel, A. Narayanasamy, and W. D. Nix, J. Mater. Res. **5**, 1073 (1990).
[17] R. W. Siegel, S. Ramasamy, H. Hahn, Z. Li, T. Lu, and R. Gronsky, J. Mater Res. **3**, 1367 (1988).
[18] R. L. Coble, J. Appl. Phys. **34**, 1671 (1963).
[19] G. W. Nieman, J. R. Weertman, and R. W. Siegel, Scr. Metall. **23**, 2013 (1989).
[20] G. W. Nieman, J. R. Weertman, and R. W. Siegel, Scr. Metall. **24**, 145 (1990).
[21] R. Birringer, H. Gleiter, H. P. Klein, and P. Marquardt, Phys. Lett. A **102**, 365 (1984).
[22] G. M. Chow, R. L. Holtz, A. Pattnaik, A. S. Edelstein, T. E. Schlesinger, and R. C. Cammarata, Appl. Phys. Lett. **56**, 1853 (1990).
[23] H. Hahn and R. S. Averback, J. Appl. Phys. **67**, 1113 (1990).
[24] T. R. Jervis and T. G. Zocco, Mater. Lett. **9**, 147 (1990).
[25] S. Matsui, T. Ichihashi, M. Baba, and A. Satoh, Superlat. Microstruct. **7**, 295 (1990).
[26] K. Baba, N. Shohata, and M. Yonezawa, Appl. Phys. Lett. **54**, 2309 (1989).
[27] R. P. Andres, R. S. Averback, W. L. Brown, L. E. Brus, W. A. Goddard III, A. Kaldor, S. G. Louie, M. Moscovits, P. S. Peercy, S. J. Riley, R. W. Siegel, F. Spaepen, and Y. Wang, J. Mater. Res. **4**, 704 (1989).
[28] A. D. Zweig, J. Appl. Phys. **70**, 1684 (1991).
[29] R. Kelly and B. Braren, Appl. Phys. B **53**, 160 (1991).
[30] Yu. V. Afanas'ev, V. M. Krol, O. N. Krokhin, and I. V. Nemchinov, J. Appl. Math. Mech. **30**, 1218 (1966).
[31] Yu. V. Afanas'ev and O. N. Krokhin, Zh. Eksp. Teor. Fiz. **52**, 966 (1967) [Sov. Phys.—JETP **25**, 639 (1967)].
[32] I. M. Kozlov, G. S. Romanov, Yu. A. Stankevich, and A. V. Teterev, Heat Transfer—Sov. Res. **21**, 222 (1989).
[33] V. A. Batanov, F. V. Bunkin, A. M. Prokhorov, and V. B. Fedorov, Zh. Eksp. Teor. Fiz. **63**, 586 (1972) [Sov. Phys.—JETP **36**, 311 (1973)].
[34] H. Gai and G. A. Voth, J. Appl. Phys. **71**, 1415 (1992).
[35] J. C. S. Kools, T. S. Baller, S. T. De Zwart, and J. Dieleman, J. Appl. Phys. **71**, 4547 (1992).
[36] F. Dahmani, Phys. Fluids B **4**, 1585 (1992).
[37] R. K. Singh and J. Narayan, Phys. Rev. B **41**, 8843 (1990).
[38] Ya. B. Zel'dovich and Yu. P. Raizer, *Physics of Shock Waves and High-Temperature Hydrodynamic Phenomena,* translation edited by W. D. Hayes and R. F. Probstein (Academic, New York, 1966), Vol. I, pp. 166, 265, 444, and 195.
[39] I. M. Lifshitz and V. V. Slyozov, J. Phys. Chem. Solids **19**, 35 (1961).
[40] P. J. Roache, *Computational Fluid Dynamics* (Hermosa, Albuquerque, 1985), p. 242.
[41] F. Heinricht and O. Bostonjoglo, Appl. Surf. Sci. **54**, 244 (1992).
[42] M. Spaeth and M. Stuke, Appl. Surf. Sci. **54**, 237 (1992).
[43] H. Wang, A. P. Salzberg, and B. R. Weiner, Appl. Phys. Lett. **59**, 935 (1991).
[44] Y. Nishikawa, Y. Yoshida, and K. Tanaka, Jpn. J. Appl. Phys. **31**, L524 (1992).
[45] M. Tadashi, S. Akiko, T. Takeshi, I. Yohichi, and G. Naoki, J. Iron Steel Inst. Japan **77**, 1851 (1991).
[46] H. Stafast and M. V. Przychowski, Appl. Surf. Sci. **36**, 150 (1989).